

## Topology optimization for stationary fluid–structure interaction problems using a new monolithic formulation

Gil Ho Yoon<sup>\*,†,‡</sup>

*School of Mechanical Engineering, Kyungpook National University, Daegu, Korea*

### SUMMARY

This paper outlines a new procedure for topology optimization in the steady-state fluid–structure interaction (FSI) problem. A review of current topology optimization methods highlights the difficulties in alternating between the two distinct sets of governing equations for fluid and structure dynamics (hereafter, the fluid and structural equations, respectively) and in imposing coupling boundary conditions between the separated fluid and solid domains. To overcome these difficulties, we propose an alternative monolithic procedure employing a unified domain rather than separated domains, which is not computationally efficient. In the proposed analysis procedure, the spatial differential operator of the fluid and structural equations for a deformed configuration is transformed into that for an undeformed configuration with the help of the deformation gradient tensor. For the coupling boundary conditions, the divergence of the pressure and the Darcy damping force are inserted into the solid and fluid equations, respectively. The proposed method is validated in several benchmark analysis problems. Topology optimization in the FSI problem is then made possible by interpolating Young's modulus, the fluid pressure of the modified solid equation, and the inverse permeability from the damping force with respect to the design variables. Copyright © 2009 John Wiley & Sons, Ltd.

Received 26 March 2009; Revised 30 July 2009; Accepted 22 September 2009

KEY WORDS: fluid–structure interaction; monolithic approach; topology optimization

### 1. INTRODUCTION

A new computational procedure is presented for topological optimization in small-deformation fluid–structure interaction (FSI) problems. Since its introduction, topology optimization has found application in many fields of engineering as well in the applied sciences [1–13]. In contrast to size and shape optimizations, topology optimization can be used to change the topologies inside design

\*Correspondence to: Gil Ho Yoon, School of Mechanical Engineering, Kyungpook National University, Daegu, Korea.

<sup>†</sup>E-mail: ghy@knu.ac.kr

<sup>‡</sup>Assistant Professor.

domains and to find optimal layouts without the need for an initial given topology. Several efforts have been devoted particularly to developing topological optimization methods for multiphysics systems such as thermomechanical, electromechanical, and acoustic-structures [2–5, 7, 10, 13–15]. As an extension of these efforts, this paper presents a new numerical analysis procedure for the steady-state FSI problem and a new optimization procedure based on it. One important aspect that we must emphasize here is that the new analysis method, although not computationally efficient, can still be used as a basis for topology optimization for a FSI problem.

Attempts have been made to use topology optimization to control fluid flow by designing the spatial distribution of the inverse permeability or porosity in the fluid domain.<sup>§</sup> The unique idea in these previous works was the assignment of a large value of inverse permeability to simulate rigid body surfaces using an artificial porous material. Numerically, it is possible to make the speed of the fluid zero (or almost zero) for no-slip boundary conditions by assigning an artificial impervious porous material. An overview with explanations of the advantages and drawbacks of this method are provided in [15, 32–36]. Attempts have also been made to optimize the fluid domain on the basis of explicit boundaries, which are parameterized interaction boundaries between solid and fluid, through the level set method [37–39]. The pressure-loaded structures are described in [8, 9].

FSI problems can be categorized into steady-state and dynamic (transient) fluid problems. Although transient systems are more common in real engineering applications, only the steady-state FSI problem is considered here to reduce the complexity of computation [16]. In FSI analysis, a staggered or monolithic analysis method with separated analysis domains is generally used, depending on how the state variables in the governing equations for fluid and the structural dynamics are coupled as shown in Figure 1 [17–31]. One of the main features of these analysis methods is the separation of the fluid domain from the structural domain. A fluid solver calculates the velocities and pressure commonly using the Navier–Stokes equation in the fluid domain and transfers this pressure load on to predefined, explicit interaction boundaries between the fluid and the structural domains. A structural solver calculates the structural displacements and transfers these displacements back to the fluid solver in order to update the fluid domain as well as the explicit interaction boundaries, which normally have no-slip boundary conditions. Most of the state-of-the-art commercial FE and fluid packages provide functions and macros to deal with these coupling conditions systematically. Size and shape optimizations have been frequently conducted using these staggered or monolithic analysis methods with separated design domains [28–31, 37–40]. By changing the profiles of the fluid and structure iteratively, an optimal size and shape can be obtained. However, methods with separated domains cannot be easily combined with topology optimization. One of the main difficulties is that the distinct fluid and structural domains and the coupling boundary conditions should be interpolated in every iteration by spatially defined design variables, as shown in Figure 2. Furthermore, in topology optimization, numerical methods to formulate the coupling boundary conditions of the governing equations for intermediate design variables are not well studied.

To make it possible to conduct topological optimization in the steady-state FSI problem, this paper presents a new monolithic analysis method employing a unified analysis and design domain. Unlike the other numerical analysis methods in Figure 2, this analysis method does not separate

<sup>§</sup>To discuss the aspects of *FSI analyses* as a whole is beyond the scope of the paper. Thus, we pay scant attention to the *optimization for FSI* with a new monolithic approach in a unified domain. For more details for analysis, see [16–31] and the references therein.

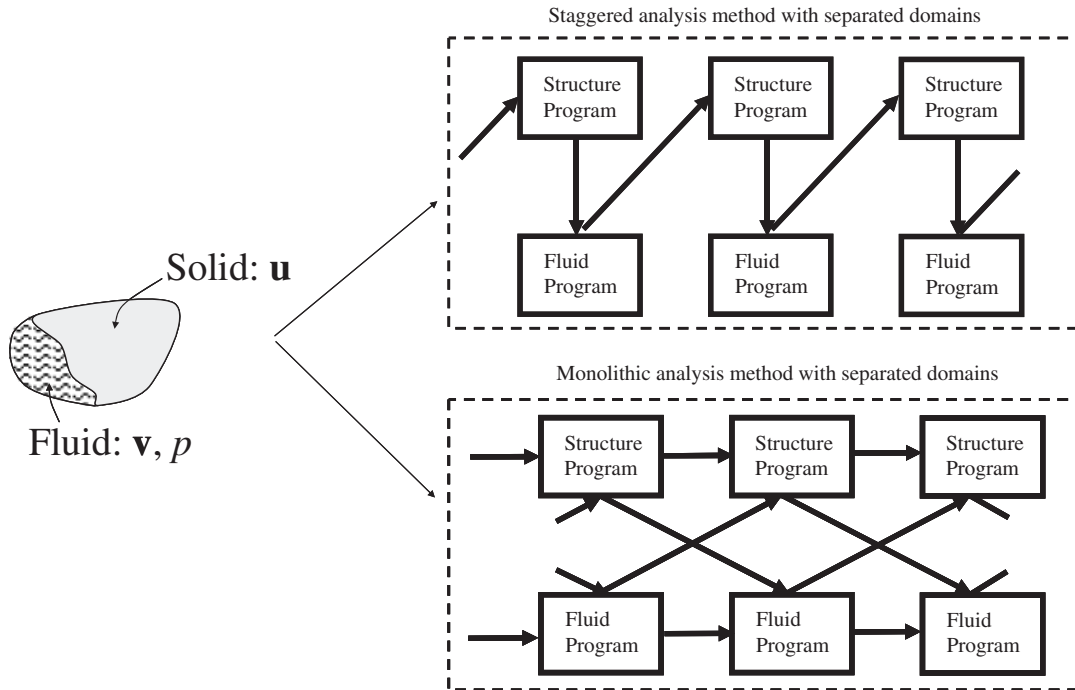


Figure 1. The staggered and monolithic analysis method with separated analysis domains.

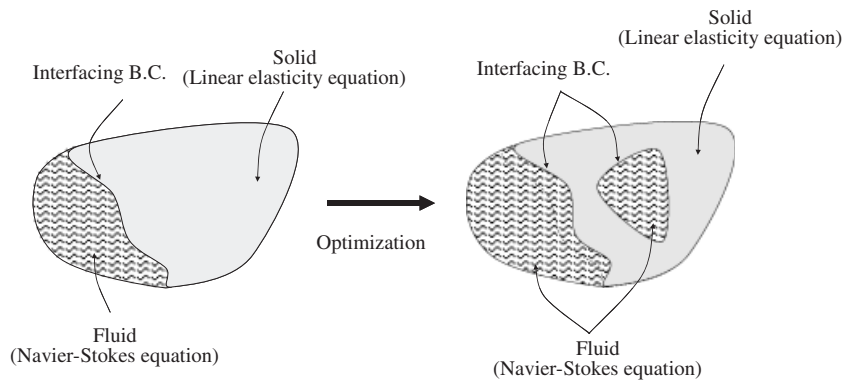


Figure 2. The changes of a topology and associated multiphysics.

the fluid and structural domains, but simultaneously describes them within a unified analysis domain. The concept behind the present monolithic analysis approach is very similar to that for the electromechanical coupling presented in [2]. Using continuum mechanics theory, the structural deformation-dependent Navier–Stokes equation is re-defined in an undeformed domain. Then, by interpolating the material properties such as the inverse of the permeability, pressure tensor, and

Young's modulus with respect to the design variables, topological optimization for steady-state FSI problems can be carried out.

In this paper, after establishing the Navier–Stokes equation and the linear elasticity equation coupled with the fluid, we develop our new monolithic approach in a unified domain. The new method is then validated by solving several benchmark problems. Some features of the new analysis method are then compared with those of existing analysis methods. Subsequently, the essential interpolation functions for the material properties and the computational complexity are investigated with several numerical examples of topology optimization applied to two-dimensional FSI problems. Finally, our findings and some topics for future research are summarized and discussed.

## 2. A MONOLITHIC APPROACH FOR THE STEADY-STATE FSI PROBLEM

Before describing the new monolithic computational approach for FSI problems, the governing equations and their associated interaction boundary conditions for FSI problems shall be circumstantially presented in this section.

### 2.1. The summary of FSI problem

**2.1.1. Basic notations and approach.** This study employed the finite element method (FEM) for FSI problem [40–42]; it is also possible to solve fluid problems by the finite volume method (FVM) or the finite difference method (FDM). To simplify the problem, the following assumptions were made:

1. The incompressible fluid and structure are at steady state. Consequently the dynamic and kinematic coupling conditions between fluid and structure can be neglected.
2. The control volumes of a fluid domain before and after structural deformation shall be distinguishable. There are two Eulerian descriptions of a fluid domain before and after structural deformations. As shown in Figure 2, these two control volumes and the coupling boundaries should be tracked during analysis.
3. Only small structural displacements are assumed for the engineering strain. However, the fluid-induced force in the linear elasticity equation is dependent on the structural displacements.

The relationship between the coordinates of the undeformed domain  ${}_{(\bigcirc)}^0\Omega$  and the deformed domain  ${}_{(\bigcirc)}^t\Omega$  (where  $\bigcirc = f$  for fluid and  $\bigcirc = s$  for structure, respectively) are given by

$$\mathbf{x} = \mathbf{X} + \mathbf{u} \quad (1)$$

where  $\mathbf{x} = \{x_i\}$  and  $\mathbf{X} = \{X_i\}$  ( $i = 1, 2$  for 2D and  $i = 1, 2, 3$  for 3D) are coordinates in the deformed and un-deformed domains, respectively. The structural displacements are denoted by  $\mathbf{u}$ .

With the above definition, the finite deformation tensor,  $\mathbf{F}$ , is defined as the partial differentiation of the current coordinate  $\mathbf{x}$  with respect to the undeformed coordinate  $\mathbf{X}$ . Indeed, the differential operators of the two configurations can be related as follows:

$$\mathbf{F} = \frac{\partial \mathbf{x}}{\partial \mathbf{X}}, \quad \nabla_{\mathbf{X}} = \mathbf{F}^T \nabla_{\mathbf{x}}, \quad \nabla_{\mathbf{x}} = \mathbf{F}^{-T} \nabla_{\mathbf{X}} \quad (2)$$

With the third assumption of small deformation in the linear elasticity equation, the above deformation tensor,  $\mathbf{F}$ , is neither used to formulate Cauchy's stress nor the engineering strain. However, it would be used to formulate the fluid-induced force which is a structural displacement-dependent load in the later equations from (26) to (29).

**2.1.2. The Navier–Stokes equation: governing equation for flow.** The steady-state Navier–Stokes equation and the incompressibility constraint of the Eulerian formulation are described as follows:

$$\rho(\mathbf{v} \cdot \nabla_{\mathbf{x}})\mathbf{v} = \nabla_{\mathbf{x}} \cdot \mathbf{T}_f \quad \text{in } {}^t\Omega(\mathbf{u}) ({}^t\Omega(\mathbf{u}): \text{fluid domain}) \quad (3)$$

$$-\nabla_{\mathbf{x}} \cdot \mathbf{v} = 0 \quad \text{in } {}^t\Omega(\mathbf{u}) \quad (\text{Fluid density } \rho = \text{constant}) \quad (4)$$

where the fluid velocity field and pressure of incompressible flow are described by  $\mathbf{v}$  and  $p$ , respectively. The derivative  $\nabla_{\mathbf{x}}$  at the time  $t$  is defined at the control volume  ${}^t\Omega(\mathbf{u})$  whose boundaries are dependent on the structural displacements  $\mathbf{u}$ . The fluid symmetric stress  $\mathbf{T}_f$ , i.e. the stress in the deformed fluid configuration, is given in the following equation:

$$\mathbf{T}_f = -p\mathbf{I} + \mu(\nabla_{\mathbf{x}}\mathbf{v} + \nabla_{\mathbf{x}}\mathbf{v}^T) \quad (5)$$

where the dynamic viscosity is  $\mu$  for the Newtonian flow. Generally, it is assumed that the fluid control volume at time  $t$ ,  ${}^t\Omega(\mathbf{u})$ , has the following boundary conditions:

$$\text{Pressure boundary condition: } \mathbf{T}_f \cdot \mathbf{n} = p_p^* \mathbf{n} \quad \text{on } {}^t\Gamma_{p^*}(\mathbf{u}) \quad (p_p^*: \text{the applied pressure}) \quad (6)$$

$$\text{No-slip boundary condition: } \mathbf{v} = \mathbf{0} \quad \text{on } {}^t\Gamma_{\mathbf{v}^0}(\mathbf{u}) \quad (7)$$

$$\text{Inflow/outflow boundary condition: } \mathbf{v} = \mathbf{v}^* \quad \text{on } {}^t\Gamma_{\mathbf{v}^*}(\mathbf{u}) \quad (8)$$

$$\text{Interfacing boundary condition: } \mathbf{v} = \frac{d\mathbf{u}}{dt} (\equiv \mathbf{0} \text{ for steady-state flow}) \quad \text{on } {}^t\Gamma_i(\mathbf{u}) \quad (9)$$

The Dirichlet boundary conditions are imposed on  ${}^t\Gamma_{\mathbf{v}^*}$  for a prescribed velocities ( $\mathbf{v}^*$ ) and  ${}^t\Gamma_{\mathbf{v}^0}$  for  $\mathbf{v} = \mathbf{0}$ , respectively. The Dirichlet boundary condition of interaction boundaries ( $\mathbf{v} \equiv \mathbf{0}$ ) is also imposed on  ${}^t\Gamma_i(\mathbf{u})$ . The Neumann boundary condition for the applied pressure  $p_p^*$  is defined at  ${}^t\Gamma_{p^*}(\mathbf{u})$  with the normal vector  $\mathbf{n}$ . Using the principle of the virtual work, the weak forms of the above equations for the virtual velocity,  $\delta\mathbf{v}$ , and the virtual pressure,  $\delta p$ , can be solved by FEM.

**2.1.3. Linear elasticity equation.** Without body force, the linear elasticity equation is formulated with Cauchy's stress,  $\mathbf{T}_s$ , in the deformed structural domain  ${}^t\Omega(\mathbf{u})$ .

$$\nabla_{\mathbf{x}} \cdot \mathbf{T}_s = \mathbf{0} \quad \text{in } {}^t\Omega(\mathbf{u}) \quad ({}^t\Omega(\mathbf{u}): \text{structural domain}) \quad (10)$$

$$\mathbf{S} = \frac{1}{2}(\nabla_{\mathbf{x}}^T \mathbf{u} + \nabla_{\mathbf{x}} \mathbf{u}), \quad \mathbf{T}_s = \mathbf{C}\mathbf{S} \quad (11)$$

where the linear strain  $\mathbf{S}$  and associate stress  $\mathbf{T}_s$  are defined as in Equation (11). The constitutive matrix is denoted by  $\mathbf{C}$ .

The Dirichlet and Neumann boundary conditions are then applied.

$$\mathbf{n} \cdot \mathbf{T}_s = \mathbf{n} \cdot \mathbf{T}_f \quad \text{on } {}^t\Gamma_i(\mathbf{u}) (= {}^t\Gamma_i(\mathbf{u})) \quad (\text{interfacing boundary condition}) \quad (12)$$

$$\mathbf{u} = \mathbf{u}^* \quad \text{on } {}^t\Gamma_{\mathbf{u}^*} \quad (13)$$

where a prescribed displacement is  $\mathbf{u}^*$  on  ${}^t\Gamma_{\mathbf{u}^*}$ .

Using the principle of virtual displacements, the following weak form can be derived:

$$\text{Linear elasticity equation: } \int_{{}^t\Omega} \delta \mathbf{S}^T \mathbf{T}_s d\Omega = - \int_{{}^t\Gamma_i} \delta \mathbf{u}^T (\mathbf{n} \cdot \mathbf{T}_f) d\Gamma \quad (14)$$

With the assumption of geometrically linear analysis, Equation (14) can be simplified into Equation (15).

$$\text{Linear elasticity equation: } \underbrace{\int_{{}^0\Omega} \delta \mathbf{S}^T \mathbf{T}_s d\Omega}_{\substack{\text{Geometrically linear} \\ (\nabla \mathbf{x} = \nabla \mathbf{x})}} = - \underbrace{\int_{{}^t\Gamma_i} \delta \mathbf{u}^T (\mathbf{n} \cdot \mathbf{T}_f) d\Gamma}_{\substack{\text{Deformation-dependent load} \\ (\nabla \mathbf{x} \neq \nabla \mathbf{x})}} \quad (15)$$

As observed in [2, 42], it is known that the coupling force of Equation (15) is contingent upon the structural displacements ( $\mathbf{u}$ ), because  $\mathbf{T}_f$  is also contingent upon the structural displacements.

Using a coupling solver, shown in Figure 1, for the fluid equations and for solid equations, the final state variables,  $\mathbf{u}$ ,  $\mathbf{v}$ , and  $p$  can be calculated. State-of-the-art commercial software such as ANSYS and ADINA provides internal subroutines to allow end-users to perform this staggered analysis for FSI problems [17, 18, 40].

Similar to acoustic-structure and electrostatic problems [2, 10, 12, 13], the element density-based topological optimization for FSI problems becomes arduous within the framework of separated-domain methods with explicit boundaries. That is because this kind of analysis methods requires predefined explicit interfacing boundary descriptions for the coupling boundary conditions. Thus, it is necessary to devise a new computational theory to overcome this limitation and to allow layout optimizations without predefined explicit boundaries between fluid and solid domains.

There is an alternative numerical analysis method called the Immersed Boundary Method or the Immersed FEM in fictitious domain as shown in Figure 3. This method uses a unified domain for fluid and structural domains and applies the artificial force, inserted in the Navier–Stoke equation as shown in Figure 3, to impose the coupling boundary condition [28–30]. Since explicit coupling boundaries can evolve in fictitious domain, the Immersed FEM has many advantages from a computational point of view. Furthermore, recently there are some researches using the Brinkman penalization in the framework of IBM [14, 43, 44]. However, this method also requires explicit boundaries between solid and fluid to impose the coupling boundary conditions, making the element density-based topology optimization difficult. However, it may be possible to design optimal structure in the framework of the level set using these analysis methods which allow optimization with separated domains.

## 2.2. The present monolithic approach interpolating fluid and structural governing equations

This section presents a new monolithic formulation for steady FSI problem. One of the main differences compared with other analysis methods is that this method does not separate the solid and fluid domains; rather a unified domain,  ${}^t\Omega(\mathbf{u})$ , is employed as shown in Figure 4.

$$\rho(\mathbf{v} \cdot \nabla_{\mathbf{x}})\mathbf{v} = \nabla_{\mathbf{x}} \cdot \mathbf{T}_f + \mathbf{F}_{FSI}$$

$$\mathbf{F}_{FSI} = \begin{cases} \mathbf{0} & \text{in } {}_f'\Omega(\mathbf{u}) \\ (\rho_f - \rho_s)(\mathbf{v} \cdot \nabla_{\mathbf{x}}\mathbf{v}) + \nabla_{\mathbf{x}}p - \mu\Delta_{\mathbf{x}}\mathbf{v} & \text{in } {}_s'\Omega(\mathbf{u}) \end{cases}$$

(a)

$$\mathbf{n} \cdot \mathbf{T}_s = \mathbf{n} \cdot \mathbf{T}_f$$

(b)

Figure 3. The concepts of the immersed boundary method (IBM) or the immersed finite element method (IFEM) which require explicit boundaries between two domains. (a) The fluid domain equation and (b) the structure domain equation.

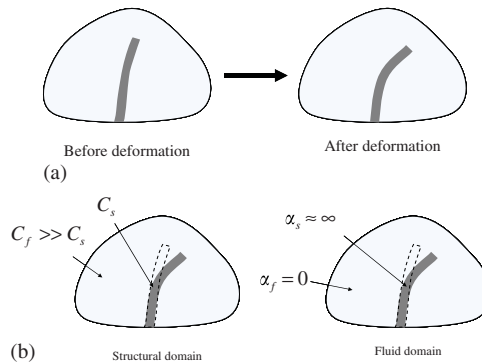


Figure 4. The essential concepts used for the present topology optimization for the stationary fluid–structure interaction problem without explicit interaction boundaries. (a) Deformed and undeformed states and (b) material values for structural domain and fluid domains (where  $C_s$  and  $C_f$  are Young's moduli for structure and fluid. The inverse coefficients of the permeability for solid and fluid are denoted by  $\alpha_s$  and  $\alpha_f$ , respectively.)

**2.2.1. Re-interpretation of the interfacing boundary conditions (continuity in velocity).** In order to derive a new monolithic approach for the FSI problem, the necessary boundary conditions applied to fluid domain must be reconsidered. On the interfacing boundaries ( ${}_f^t\Gamma_i(\mathbf{u})$  or  ${}_s^t\Gamma_i(\mathbf{u})$ ) between fluids and solids, it is essential that the velocities of the steady-state fluid should satisfy the no-slip boundary condition

$$\mathbf{v} \equiv \mathbf{0} \quad (\text{at the no-slip boundary}) \quad (16)$$

The genius idea of using the inverse permeability to simulate the above no-slip boundary condition for topology optimization was proposed in [32–34]. To this end, several research papers modified the Navier–Stokes equation by inserting Darcy's damping force and this novel concept

for the present approach was also employed [32–34].

$$\rho(\mathbf{v} \cdot \nabla_{\mathbf{x}}) \mathbf{v} = \nabla_{\mathbf{x}} \cdot \mathbf{T}_f - \underbrace{\alpha \mathbf{v}}_{\text{Friction force}} \quad \text{in } {}^t\Omega(\mathbf{u}) \quad (17)$$

$$-\nabla_{\mathbf{x}} \cdot \mathbf{v} = 0 \quad \text{in } {}^t\Omega(\mathbf{u}) \quad (18)$$

where  $\alpha$  is the inverse coefficient of permeability of the fluid. It is obvious that velocities become almost zero alongside with a large number of  $\alpha(\alpha_{\max})$ . Therefore, the following conditions can be devised:

$$\begin{aligned} \alpha &= \alpha_{\max} \gg 0 \quad \text{for solid or non-fluid} \\ \alpha &= 0 \quad \text{for fluid} \end{aligned} \quad (19)$$

It is possible to change or interpolate this coefficient at each point of a design domain to optimize flow channels [33].

Since the order of magnitude of  $\alpha_{\max}$ , the inverse of permeability of a porous solid, determines how impervious material is, it merits the development of a guideline on how to choose a proper value in the above equations. With a  $\alpha_{\max}$  value too small, solid models allow water to go through while a too high number can lead to a numerical singularity. For fluid optimization problems, through extensive studies, the following criterion was proposed in [33, 35, 36]. This criterion was also tested and followed for the FSI problem in this study.

$$\alpha_{\max} = \frac{\mu}{D_a L_c^2} \quad (20)$$

where  $D_a$  is Darcy's number and  $L_c$  is the characteristic length. To determine whether a chosen value was sufficient or not, several Darcy's numbers were numerically tested in the example section as well as in the analysis example section.

**2.2.2. Re-interpretation of the interfacing boundary conditions (continuity in traction).** To satisfy the continuity in traction, the traction forces defined by the surface integral of the fluid pressure shall be converted as the body force using the formulation of the divergence theory of Green.

$$\underbrace{\int_{ms} {}^t\Omega \nabla_{\mathbf{x}} \cdot \mathbf{T}_f d\Omega}_{\text{Present approach}} = \underbrace{\int_s {}^t\Gamma_i \mathbf{n}^T \mathbf{T}_f d\Gamma}_{\substack{\text{previous methods} \\ \text{with explicit boundary}}} \quad (21a)$$

$${}^t\Omega = {}_{ms}^t\Omega \cup {}_{mf}^t\Omega \quad (21b)$$

where  ${}_{ms}^t\Omega$  and  ${}_{mf}^t\Omega$  are domains for solid structure and fluid in the unified domain  ${}^t\Omega$ , respectively. Note that the integral of the divergence of the fluid stress should be only defined at  ${}_{ms}^t\Omega$  not  ${}_{mf}^t\Omega$ .

By inserting the above equation into Equation (15), the linear elasticity equation having the fluid interaction force as the body force is derived [39].

$$\nabla_{\mathbf{x}} \cdot \mathbf{T}_s = \nabla_{\mathbf{x}} \cdot \mathbf{T}_f \quad \text{in } {}_{ms}^t\Omega \quad (22)$$



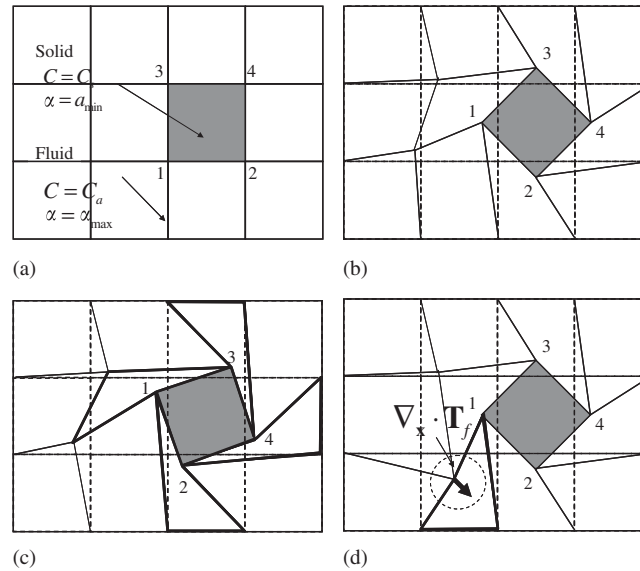


Figure 5. The limitation of the small displacements. (a) Undeformed state ( $C_s$  and  $C_a$  : Young's modulus for solid and void); (b) deformed state with small displacements; (c) deformed state with large displacements (Degenerated mesh); and (d) an example of the need of the restriction of the fluid force with  $\Psi$ .

Since the above equation is only valid at the solid domain  ${}^t\Omega_{ms}$ , the above derivation also requires the explicit boundaries between  ${}^t\Omega_{ms}$  and  ${}^t\Omega_{mf}$ , that is an un-desirable feature. Therefore, we reformulate the Equation (22) as follows (see Figures 5 and 6).

$$\nabla_{\mathbf{x}} \cdot \mathbf{T}_s = \Psi \times (\nabla_{\mathbf{x}} \cdot \mathbf{T}_f) \quad \text{in } {}^t\Omega(\mathbf{u}) \quad (23)$$

$$\Psi = \begin{cases} 1 & \text{for solid} \\ 0 & \text{for fluid} \end{cases} \quad (24)$$

This function does not change the forces applied to the structural domains. Furthermore, as shown in Figure 5(d) it turns out that the equation without  $\Psi$  can make large displacements and mesh distortions at the updated geometry  ${}^t\Omega(\mathbf{u})$  especially for fluid regions,  ${}^t\Omega_f$ , having a weak Young's modulus (ex.,  $10^{-9}$  times of the original Young's modulus). In this sense, the function  $\Psi$  also helps to regulate mesh distortions in fluid domains. However, even the present method can, sometimes, come to its limits in the solid domain where only a re-meshing scheme helps [20, 28–30].

Furthermore, because the velocities in the solid domain are zero, Equation (23) can finally be reformulated as follows:

$$\nabla_{\mathbf{x}} \cdot \mathbf{T}_s = -\Psi \cdot \nabla_{\mathbf{x}} p \quad \text{in } {}^t\Omega(\mathbf{u}) \quad (25)$$

Figure 7, as an illustrative example, shows that the surface integral of the pressure can be computed in a unified domain with the help of  $\Psi$ . Furthermore, the above formulation only holds for zero (very small value) or one design variables completely. Therefore, if intermediate design

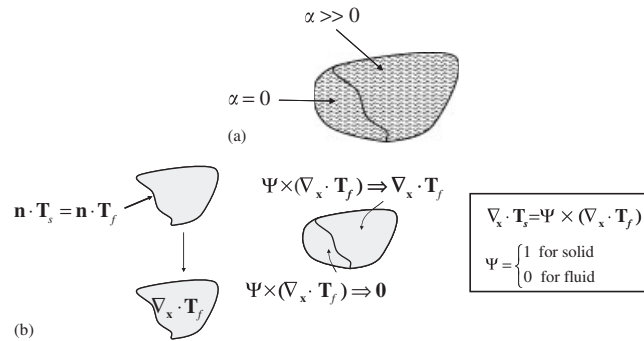


Figure 6. The inverse permeability and the fluid–structure interaction force. (a) The coefficient of inverse permeability for solid and fluid and (b) the fluid–structure interaction force in the present approach of Equations (23) and (24).

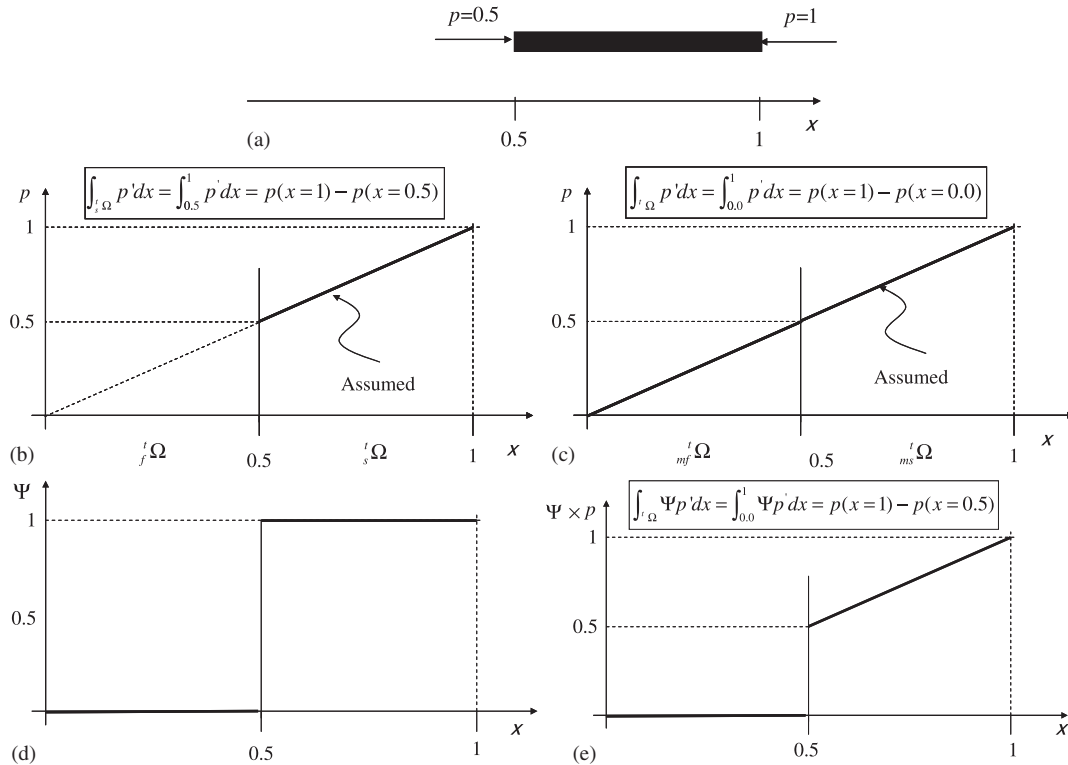


Figure 7. One-dimensional example showing the necessity of Equations (23) and (24). (a) One-dimensional element with pressures at both sides; (b) the pressure integration over the solid domain  ${}^t\Omega_s$ ; (c) the integration of the pressure gradient over  ${}^t\Omega (= {}^t\Omega_{mf} \cup {}^t\Omega_{ms})$  which gives an inconsistent result; (d) the filter function of (24); and (e) the integration of the pressure gradient time the filter over  ${}^t\Omega (= {}^t\Omega_{mf} \cup {}^t\Omega_{ms})$  which gives a consistent result.

variables  $\gamma$  appear, some other penalizations or constraints such as  $\int \gamma(1-\gamma) \, d\Omega$  should be inserted, which have not been employed here.

**2.2.3. Reformulation of Equations (17), (18), and (25) in the undeformed domain  ${}^0\Omega(\mathbf{u})$ .** Up to this point, these three equations (17), (18), and (25) still contain integrations in  ${}^t\Omega(\mathbf{u})$  that require an updating of their geometries. To tackle this, we used the transformation of the differential operators. In other words, the two governing equations are redefined in the undeformed domain using Equations (2) and (26) as follows:

$$\nabla_{\mathbf{x}}\mathbf{u}=\mathbf{F}^{-T}\nabla_{\mathbf{X}}\mathbf{u}, \quad \nabla_{\mathbf{x}}\mathbf{v}=\mathbf{F}^{-T}\nabla_{\mathbf{X}}\mathbf{v} \quad \text{and} \quad \int_{\Omega}() \, d\Omega = \int_{{}^0\Omega}() \|\mathbf{F}\| \, d\Omega \quad (26)$$

$$\begin{aligned} - \int_{{}^0\Omega} \delta \mathbf{v}^T \{ \rho (\mathbf{v} \cdot \mathbf{F}^{-T} \nabla_{\mathbf{X}} \mathbf{v}) \} \|\mathbf{F}\| \, d\Omega &= \int_{{}^0\Omega} \mathbf{F}^{-T} \nabla_{\mathbf{X}} \delta \mathbf{v}^T \mathbf{T}_f \|\mathbf{F}\| \, d\Omega \\ &+ \int_{{}^0\Omega} \alpha \delta \mathbf{v}^T \mathbf{v} \|\mathbf{F}\| \, d\Omega - \int_{{}^0\Gamma_{p^*}} p_p^* \mathbf{n} \, d\Gamma \end{aligned} \quad (27)$$

$$- \int_{{}^0\Omega} \delta p^T \{ (\nabla_{\mathbf{x}} \cdot \mathbf{v}) \} \|\mathbf{F}\| \, d\Omega = 0 \quad (28)$$

$$\int_{{}^0\Omega} \delta \mathbf{S}^T \cdot \mathbf{T}_s \, d\Omega = \int_{{}^0\Omega} \delta \mathbf{u} \cdot \Psi \cdot (\mathbf{F}^{-T} \nabla_{\mathbf{X}} p) \|\mathbf{F}\| \, d\Omega \quad (29)$$

The above formulations are inefficient from a computational points of view due to redundant degrees of freedom of the linear elasticity equation in the fluid domain and those of the Navier–Stokes equation in the solid domain. However, these redundancies allow topology optimization by distributing design variables.

Unlike other FSI algorithms such as the Immersed Boundary Method in Figure 3, the present analysis does not require explicit boundary curves to define solid and fluid domain. By assigning zero (or very small value) or one to the design variable  $\gamma$  for the material properties such as Young's modulus of elasticity, fluid pressure, and the inverse permeability coefficients arising in Equations (27), (28), and (29), solid domain and fluid domain can be described as shown in Table I. Thus, this is a new monolithic approach with a unified domain for FSI problem.

Table I. Material properties of the present monolithic approach for the FSI problem.

	Linear elasticity equation		Fluid equation
	Young's modulus (C)	Penalization for fluid stress ( $\Psi$ )	Inverse permeability ( $\alpha$ )
Solid ( $\gamma=1$ )	$C_s$	1	$\alpha_{\max} \gg 0$
Fluid ( $\gamma=0$ )	$C_f \ll C_s$	0	0

where  $C_s$  and  $C_f$  are Young's moduli for the solid and fluid, respectively. Young's modulus for the fluid ( $C_f$ ) is much smaller than that for the solid ( $C_s$ ). And the design variable is denoted by  $\gamma$ .

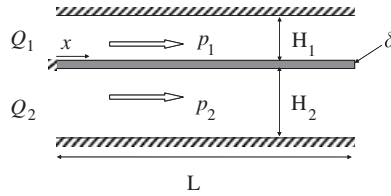


Figure 8. The mathematical model of the fluid-induced deflection. ( $H_1=0.02$  m,  $H_2=0.04$  m,  $L=0.75$  m,  $Q_1=177 \times 10^{-6}$  m<sup>3</sup> s<sup>-1</sup>,  $Q_2=354 \times 10^{-6}$  m<sup>3</sup> s<sup>-1</sup>,  $\delta=0.01$  m,  $\rho=1000$  kg/m<sup>3</sup>,  $\mu=0.001$  kg m<sup>-1</sup> s<sup>-1</sup>,  $E=2 \times 10^{11}$  N/m<sup>2</sup>,  $\nu=0.3$ ,  $Da=10^{-9}$ .)

### 2.3. Numerical analysis examples

**2.3.1. Example 1: a beam inside channels.** To verify the validity of the present monolithic formulation, we considered a channel separated with a slender beam of length  $L$  studied as shown in Figure 8 [17, 18]. Owing to the normal pressure difference induced by different flowrates,  $Q_1$  and  $Q_2$ , in the upper and the lower channel, the slender beam would be bent.

Assuming the fully developed laminar flows and constant height  $H_1$  and  $H_2$  in the channel, the analytical solutions of the pressure differences as well as the tip displacement can be derived [17, 18]. Together,

$$EI \frac{d^4 w}{dx^4} - g_1(x) \frac{d^2 w}{dx^2} + g_2(x) w = g_3(x) \quad x \in [0, L] \quad (30a)$$

$$g_1(x) = 6\mu \int_x^L \left[ \frac{Q_1}{H_1^2(s)} + \frac{Q_2}{H_2^2(s)} \right] ds \quad (30b)$$

$$g_2(x) = 36\mu \int_x^L \left[ \frac{Q_1}{H_1^4(s)} + \frac{Q_2}{H_2^4(s)} \right] ds \quad (30c)$$

$$g_3(x) = -12\mu \int_x^L \left[ \frac{Q_1}{H_1^3(s)} - \frac{Q_2}{H_2^4(s)} \right] ds \quad (30d)$$

where the deflection of the beam is denoted by  $w$  and the moment of the inertia,  $I$ , is  $h^3/12$ . By substituting  $g_1$  and  $g_2$  into Equation (30) for  $w$  on the left-hand side and  $g_3$  on the right-hand side, the deflection of the slender beam can be calculated. To find out a numerical solution of this Equation (30a), we used the method of finite differences to convert the differential operators to a set of linear algebra equations [17, 18].

Using the present monolithic formulation with the plane strain formulation, the deflection on the slender beam as well as the pressure differences on the top and bottom surfaces of the beam in Figure 9 was calculated. This experiment reveals that our results agree with those obtained by Equation (30). Figure 10 shows the streamlines, velocities, and pressure obtained by the present monolithic approach.

At this point, it may be useful to look further into some important features of the relationship between the displacement and various Darcy's numbers. To do so, we investigate the effect of varying Darcy's number on the tip displacement with reference to the point A. The result is shown

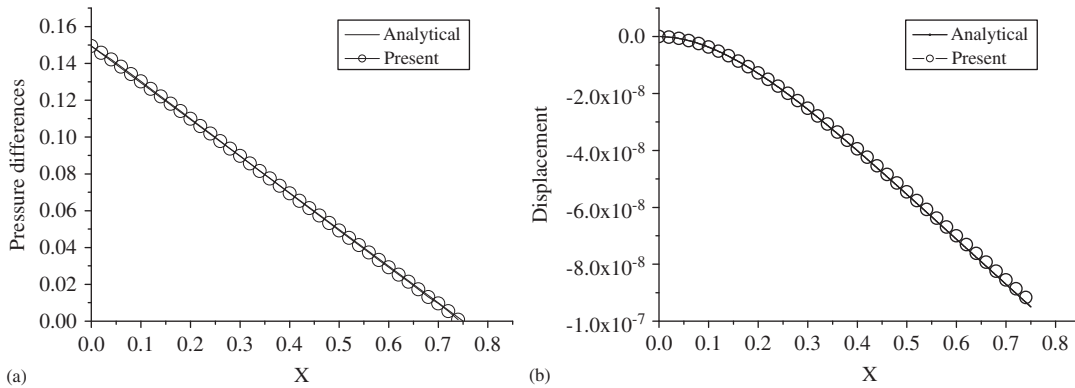


Figure 9. The comparison of solutions of the analytical method and the present monolithic method. (a) The displacements along the slender beam and (b) the induced pressure differences upon the slender beam.

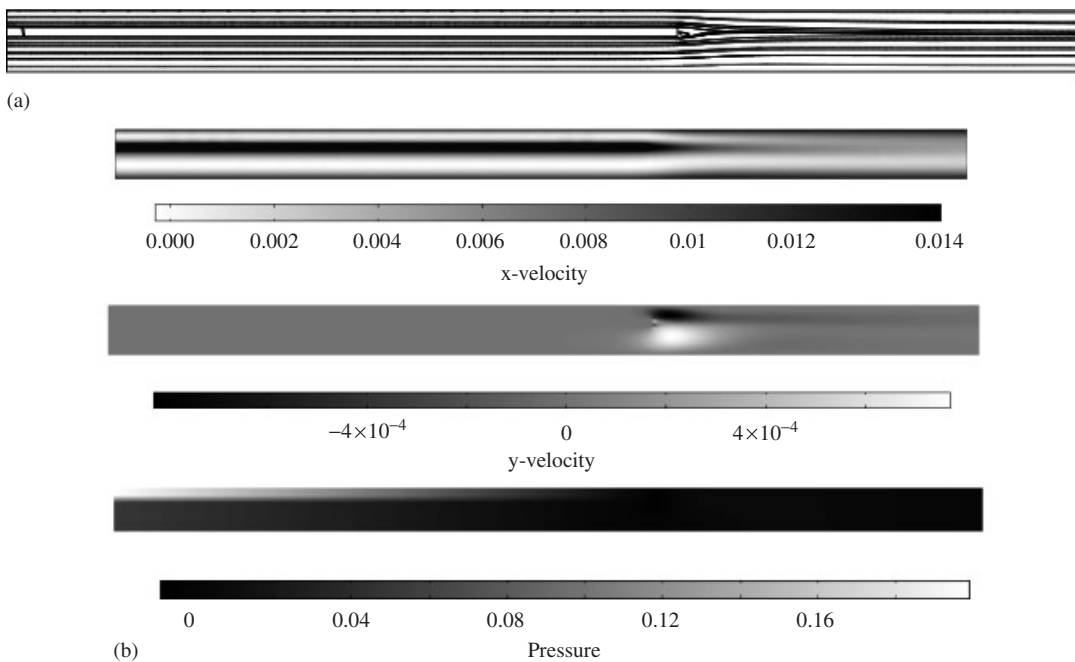


Figure 10. The solution of the present monolithic method for the model of Figure 8: (a) Flowlines and (b) velocities and pressure.

in Figure 11. It seems that it is a valid idea to use Darcy's damping force to simulate the solid part even for the FSI problem. Furthermore, it is noticed that a value around  $10^{-9}$  for  $Da$  is sufficient to make the slender beam impervious.

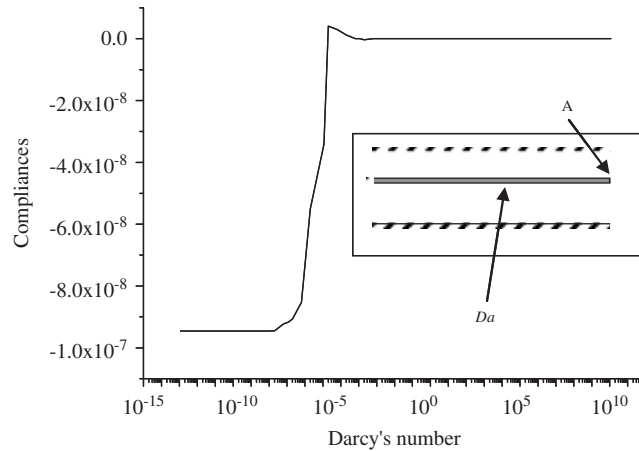


Figure 11. The tip displacement at the point A versus Darcy's numbers.

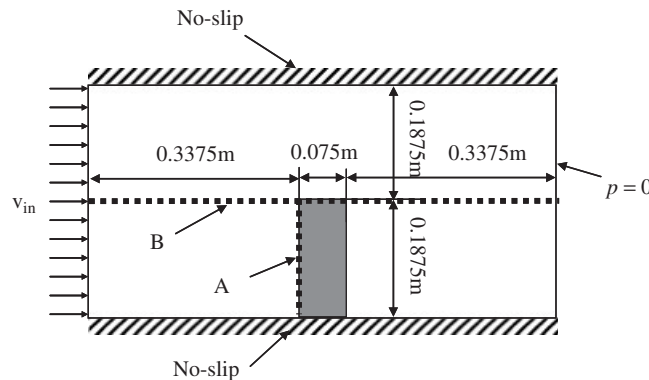


Figure 12. The model for a column inside a channel. ( $\rho = 1000 \text{ kg/m}^3$ ,  $\mu = 0.001 \text{ kg m}^{-1} \text{ s}^{-1}$ ,  $E = 2 \times 10^{11} \text{ N/m}^2$ ,  $\nu = 0.3$ ,  $V_{in} = 8.85 \times 10^{-4} \text{ m/s}$ ,  $Da = 10^{-9}$ .)

**2.3.2. Example 2: deflection of a column inside a channel.** In this analysis example, the deflection and pressure of a slender plain-strain column, which is deflected due to flow inside the channel, are compared with the solutions calculated by the state-of-the-art commercial software, ANSYS in Figure 12. Combining the FLOTRAN fluid solver and a linear structure solver, this commercial software provides a staggered analysis macro called FSSOLVE [40]. Thus it is possible to compare structural displacements and pressure distributions of two analysis methods inside the domain with various input fluid velocities.

Figure 13 shows the deflections of the column at Section A, as well as the pressure distribution at Section B. As shown in Figure 13, the present monolithic approach shows a good agreement with the state-of-the-art commercial software. In Figure 14, the relationship between the tip displacement with reference to C and Darcy's number is plotted. Similar to the first numerical example, it shows that a small Darcy's number around  $10^{-9}$  is sufficient to make the column impervious.

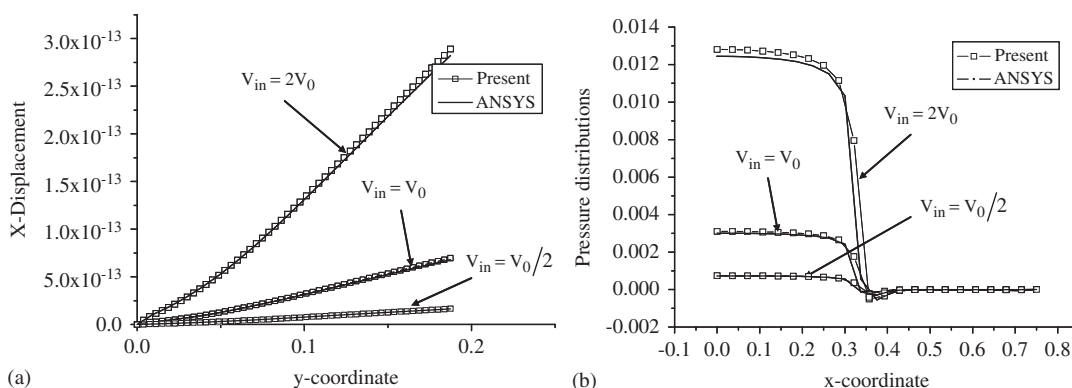


Figure 13. The comparisons of the displacements and pressure of the column inside a channel: (a) Section-A and (b) Section-B.

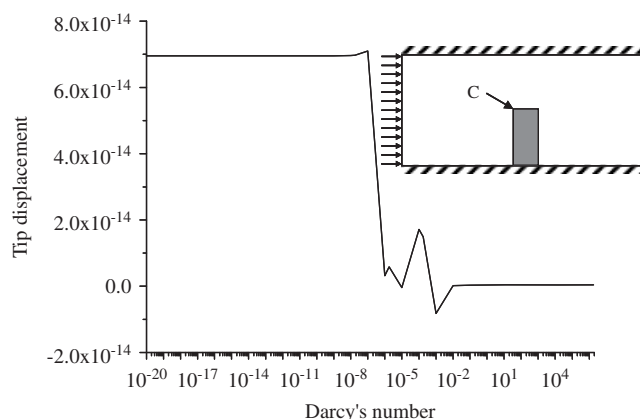


Figure 14. The tip displacement at the point C versus Darcy's numbers.

**2.3.3. Example 3: clamped beam deflection due to flow.** In this analysis example, we compared the compliances of two beams of length  $L$ , with constant cross section, and homogeneous material, with stresses induced by a fluid flow and explicit stresses equivalent to the stresses from the fluid, as shown in Figure 15.

Figure 16 compares the compliances along the beam for situations shown in Figure 15(a) and (b). With a small number for  $Da$ , the compliance from the present monolithic approach converges to the compliance value obtained by the structural model. Furthermore, to study the effects of Darcy's number, we plot the compliances with various  $Da$  in Figure 16. Clearly, with a sufficiently small number, the beam is sufficiently impervious and the calculated compliances are approaching the compliance value of the pure structure. It is also noticeable that there are some oscillations in compliance from around  $10^{-7}$  to  $10^{-5}$  because the water of the upper channel oozes out of the clamped beam [33, 35].

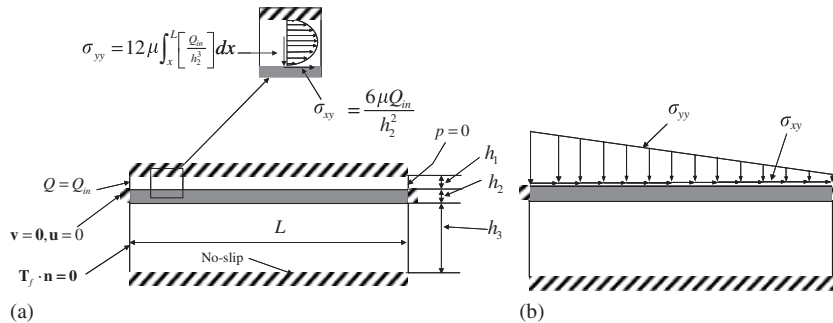


Figure 15. The compliance comparison of a beam due to flow. (a) A plain-strain model with flow ( $Q_{in}=177 \times 10^{-6} \text{ m}^3 \text{ s}^{-1}$ ,  $L=4 \times 10^{-4} \text{ m}$ ,  $h_1=2 \times 10^{-5} \text{ m}$ ,  $h_2=2 \times 10^{-5} \text{ m}$ ,  $h_3=1 \times 10^{-4} \text{ m}$ ,  $\rho=1000 \text{ kg/m}^3$ ,  $\mu=0.001 \text{ kg m}^{-1} \text{ s}^{-1}$ ,  $E=3 \times 10^{11} \text{ N/m}^2$ ,  $\nu=0.3$ ) and (b) a pure structural model with equivalent stresses.

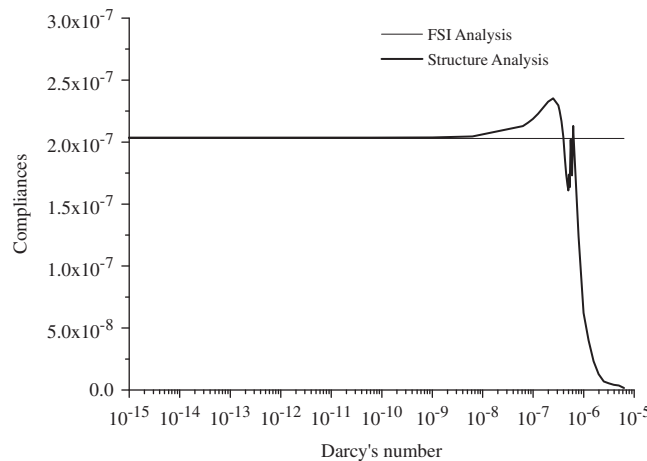


Figure 16. The compliances of the Figure 15 structure with various Darcy's numbers.

### 3. TOPOLOGY OPTIMIZATION FOR THE STATIONARY FSI PROBLEM

#### 3.1. Interpolation functions for topological optimization: interpolating the two governing equations

A typical difficulty when dealing with topological optimization is in solving the discrete optimization problem. The usual approach to resolve this difficulty is by relaxing the binary design optimization problem with continuous design variables. One popular relaxation method is the so called solid isotropic material with penalization (SIMP) method which can be used to perform optimization when combined with a mathematical method. For layout optimization for the FSI problem, the situation becomes more complicated because not only the design variables but the physics as well should be interpolated. Thus, an attempt is made to interpolate the two physics by the same relaxation approach on the basis of the numerical framework proposed in the previous



section. Assigning zero or one to the design variables for the solid and fluid domains, respectively, allows optimization without the need for explicit boundaries.

For the interpolation functions for Table I, we employ the most popular interpolation method, the SIMP approach as follows:

$$\Psi(\gamma) = (1 - 0)\gamma^{n_1} + 0 \quad (31)$$

$$C(\gamma) = (C_s - C_f)\gamma^{n_2} + C_f \quad (32)$$

$$\alpha(\gamma) = (\alpha_{\max} - 0)\gamma^{n_3} + 0 \quad (33)$$

$$0 \leq \gamma \leq 1 \quad (34)$$

where  $n_1$ ,  $n_2$ , and  $n_3$  are the penalization factors of fluid stress, Young's modulus, and the inverse permeability. For the numerical examples, we set 3 for  $n_1$ ,  $n_2$ , and  $n_3$  unless otherwise stated. Optimization results clearly converged to one and zero can be obtained by assigning different penalization factors instead of an identical penalization, as observed in Reference [33].

### 3.2. Topological optimization examples

In this section, some engineering design problems considering FSI are solved using a gradient-based optimizer, MMA [45]. The proposed approach was implemented in the frameworks of MATLAB and COMSOL because of the advantage of the sensitivity analysis. The accuracy of the sensitivity values have been numerically verified [2, 10, 46].

**3.2.1. Example 1: minimizing the compliance of a structure due to the fluid flow.** To investigate the feasibility of using the present monolithic method for topology optimization considering FSI, this first example considers the compliance minimization problem of Figure 15 considering the fluid stresses in the channel located at the top of the design domain. To obtain a reference design, we also solved the compliance minimization problem with structural stresses equivalent to the fluid stresses in Figure 15. The objective function and constraint were set as follows:

$$\begin{aligned} \text{Min} \quad & \int_{\Omega_d} \mathbf{S}^T \mathbf{T}_s \, d\Omega \\ \text{s.t.} \quad & \frac{1}{|\Omega_d|} \int_{\Omega_d} \gamma \, d\Omega - \beta \leq 0 \end{aligned} \quad (35)$$

where  $\Omega_d$  and  $\beta$  are the design domain and allowed mass ratio, respectively. The analytical sensitivity values are compared with the values from the finite difference method for some design variables in Figure 17.

Figure 18 shows the optimal layouts obtained by the present monolithic analysis and pure structural analysis with a void initial density distribution at which slight differences in topologies exist. Because the upper panel is almost impervious, the forces acting on the structures are almost identical, making it likely that similar results will be obtained. Figure 19 shows the fluid velocities and pressure distribution, as well as the resulting compliances for various input flows. In Figure 19, high pressure within the structure is due to the divergence theory of Green (See the comments for Figure 7). With this developed pressure, the external fluid force applied to the structure is transformed into the body force. The design considering FSI always shows better compliances than

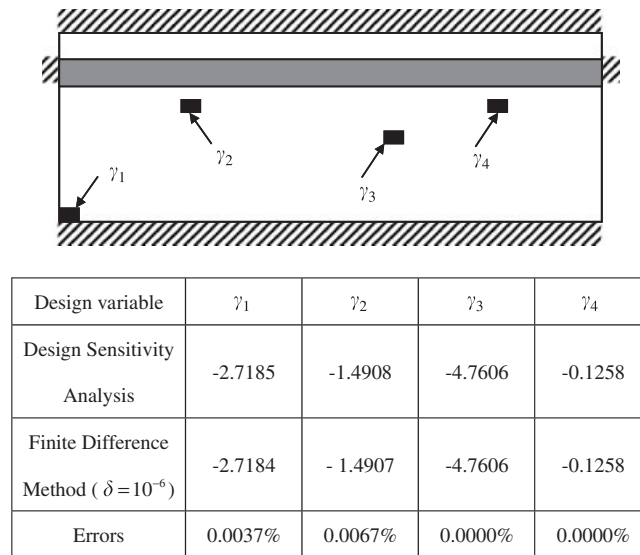


Figure 17. Sensitivity analysis check (Error = (DSA – FDM)/FDM).

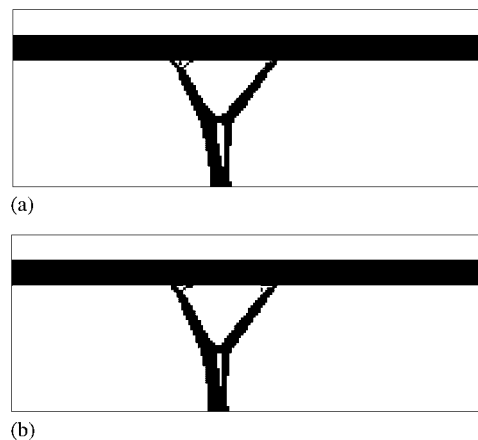


Figure 18. The results of compliance minimization problems due to the force of flow ( $\beta=5\%$ ) using (a) the present monolithic approach (FSI result (Object =  $56.26 \times 10^{-10}$  J,  $Da = 10^{-9}$ )); and (b) the pure structural model with the pressure load (pure structure (Object =  $58.68 \times 10^{-10}$  J)).

those of the layout in Figure 18(b). Figure 20 shows several numerical tests with various  $Da$  values. It is observed that larger values produce different local optima for the two structures, whereas small values produce similar results. Obviously to avoid numerical instability, an appropriate lower bound for  $Da$  and an appropriate upper bound for  $\alpha$  should be used.

**3.2.2. Example 2: minimizing pressure loss inside a channel.** In the next illustrative example, we attempt to design an internal structure that minimizes the pressure drop between the inlet and

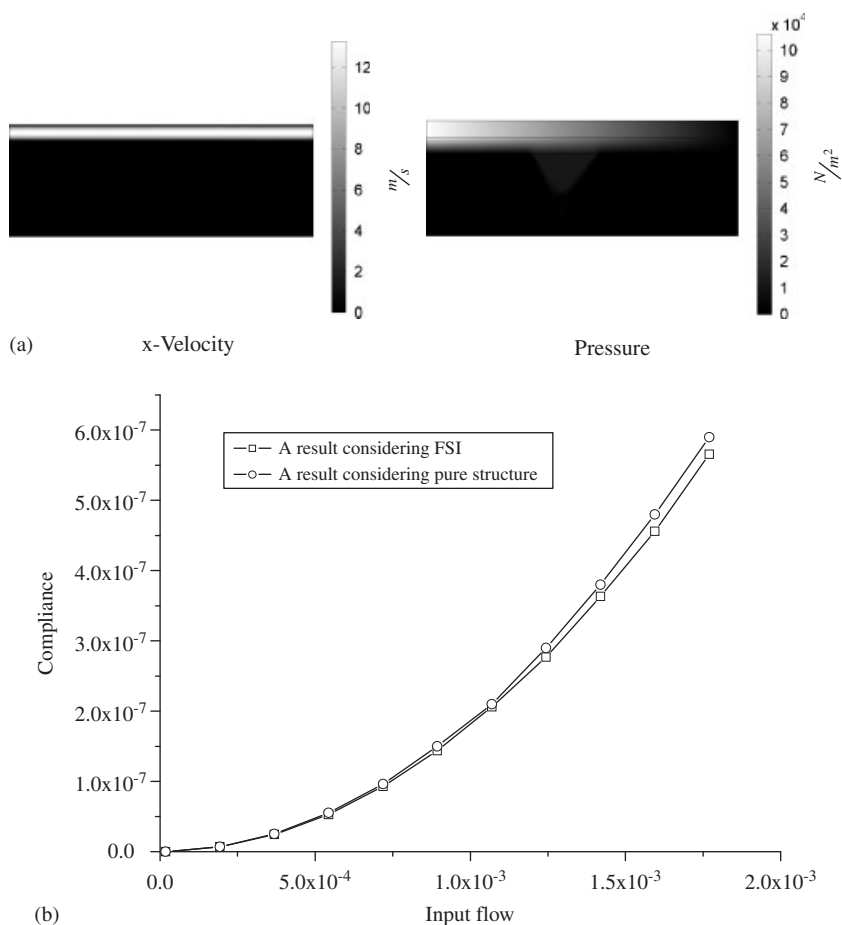


Figure 19. The compliance comparison of the obtained designs. (a) The fluid velocities and pressure of Figure 18(a) and (b) compliances of the two designs with various input flows.

outlet of the box-shaped channel shown in Figure 21. The fully developed laminar flow at the inlet is set normal to the boundary and is parabolic. Because of the uniform cross sections of the inlet and outlet, the pressure loss inside the channel is mainly determined by the internal geometry; thus the pressure drop due to the upper and lower parallel boundaries is ignored. Therefore, by minimizing the pressure drop between the inlet and outlet through topology optimization, it may be expected that an aerodynamic structure will be obtained. Figure 22(a) displays the optimized density distribution, which is similar to that of a wing section. To avoid trivial structures and ill-posedness of the governing equations, this example includes a fixed region inside the channel and employs a mass constraint of the form of Equation (36); without the fixed region and the mass constraint, a void structure is optimal. From the streamlines and pressure contour plots shown in Figure 22, it is clear that topology optimization considering FSI can produce an aerodynamic

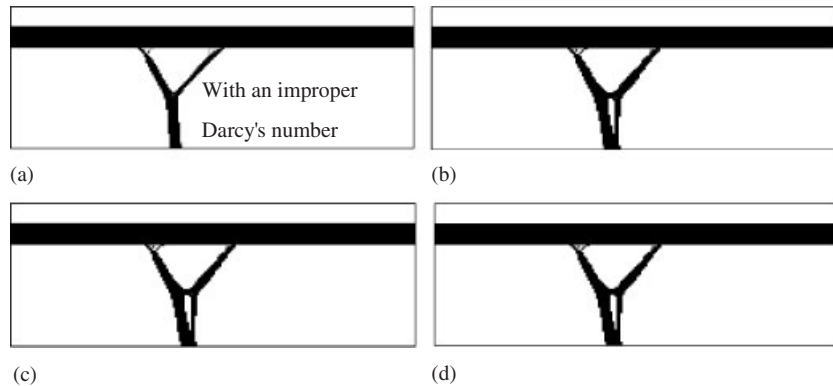


Figure 20. Numerical tests with different Darcy's values. (a) A result with an improper value  $Da=10^{-5}$  (Object  $=0.3875 \times 10^{-10}$  J); (b) a result with,  $Da=10^{-9}$  (Object  $=56.26 \times 10^{-10}$  J); (c) a result with  $Da=10^{-10}$  (Object  $=56.24 \times 10^{-10}$  J); and (d) a result with  $Da=10^{-11}$  (Object  $=56.24 \times 10^{-10}$  J).

structure that is physically acceptable.

$$\begin{aligned} \text{Min} \quad & \int_{\Omega_{\text{inlet}}} p \, d\Omega - \int_{\Omega_{\text{outlet}}} p \, d\Omega \\ \text{s.t.} \quad & \frac{1}{|\Omega_d|} \int_{\Omega_d} \gamma \, d\Omega - \beta \geq 0 \end{aligned} \quad (36)$$

### 3.2.3. Example 3: minimizing the compliance of a structure with design-dependent fluid loads.

In this numerical example, a compliance minimization problem considering the design-dependent loads produced by flow is solved, as shown in Figure 23. Since the impervious beam acts as a separator between the upper and lower fluid domains, the simple compliance minimization problem of Example 1 with the equivalent static loads from the fluid can be solved. However, since the interfacing surfaces are allowed to vary in this example, the optimal interaction surfaces should be determined by considering the design-dependent loads caused by the flow. To avoid trivial solutions or a void structure, a rectangular domain located at the center of Figure 23 was defined as a solid box with a mass constraint as in Equation (35). Figure 23(b) also shows the variation in compliances with Darcy's numbers, which is needed to determine the proper Darcy's value. Here, as in the previous examples, a small Darcy's number of around  $10^{-9}$  is sufficient.

Figures 24, 25, and 26 show some supporting structures obtained by the present approach at various fluid speeds. They show that boundaries between the solid and fluid are optimized. At very slow flowrates, a supporting structure appears in front of the solid box, whereas at relatively faster flowrates, a supporting structure appears behind the solid box because of the inertia effect. To obtain optimization results clearly converged to one and a small value, a higher penalty, 11, is used in Equation (33), which substantially reduces the effect of intermediate design variables on the inverse permeability.

To validate the present approach, the obtained design is reanalyzed with the staggering analysis method in ANSYS after manual post-processing processes; the results are shown in Figure 27.

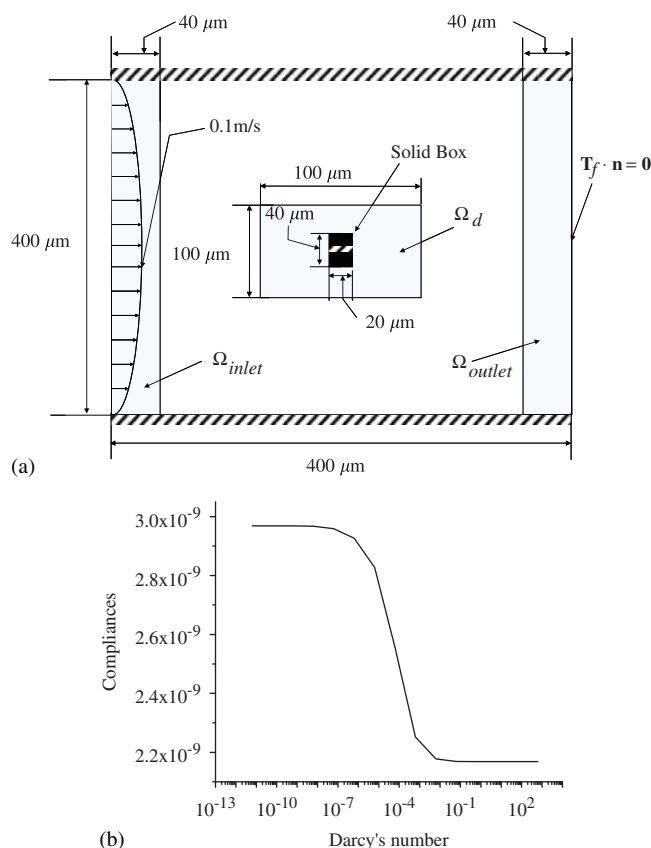


Figure 21. The problem definition of minimizing the pressure drop inside a channel. (a) The problem definition ( $\rho = 1000\text{ kg/m}^3$ ,  $\mu = 0.001\text{ kg m}^{-1}\text{ s}^{-1}$ ,  $\alpha_{\max} = 10^{12}$ ,  $E = 3 \times 10^9\text{ N/m}^2$ ,  $\nu = 0.3$ ,  $\beta = 0.5$ ) and (b) the objective curve with various  $\alpha_{\max}$ .

The calculated objective functions for the given flowrates are almost the same as those obtained by the present monolithic approach. The slight differences are due to the effects of gray elements and post-processing. Nevertheless, this comparison shows that it is possible to use the present approach to design optimal topologies considering FSI.

#### 4. CONCLUSIONS

This paper presents both a new analysis procedure and optimization formulations, paving the way for topology optimization for FSI systems. Commonly, FSI systems have been analyzed with separated fluid and solid domains by a staggering or monolithic analysis method with kinematic and dynamic coupling conditions. Although these analysis methods have some advantages in analysis and in size/shape optimization, they become prohibitively complicated when employed for density-based topological optimization. This is partially because the governing equations and the

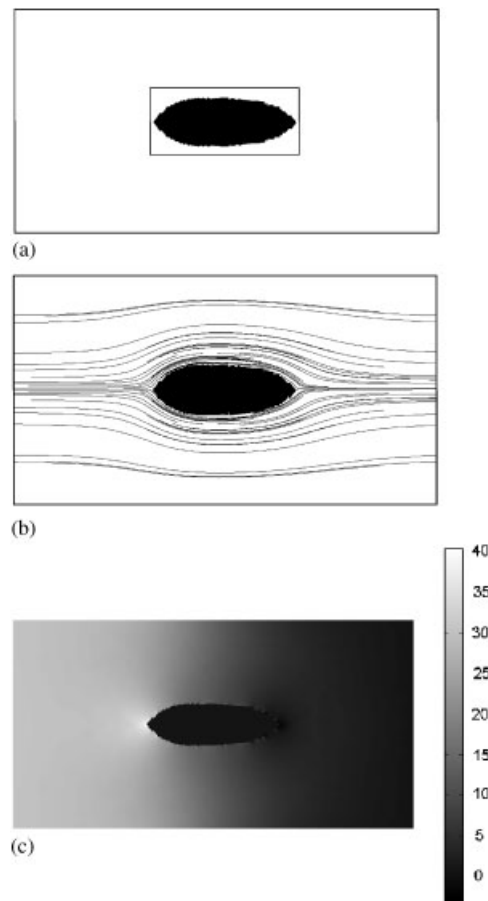


Figure 22. The obtained design by the present monolithic approach. (a) An optimized result (object =  $11.72 \times 10^{-8} \text{ N/m}^2$ ,  $Da = 10^{-9}$ ); (b) the flowlines; and (c) the pressure distribution.

associated coupling boundary conditions need to be changed on newly created holes and removed holes, which is difficult in the density-based topology optimization.

To resolve these difficulties, this paper presents a new monolithic analysis approach with a unified analysis domain having redundant fluid and solid FE meshes in the solid and fluid domains, respectively. Thus, from a computational point of view, the present analysis method is not as efficient as existing FSI analysis methods because the total number of degrees of freedom increases. However, by assigning limit values for material properties such as the inverse permeability of Darcy's damping force, Young's modulus, and the pressure filter of the linear elasticity equation, it is possible to model topological changes without explicit boundaries between the two domains. The effectiveness of the present analysis method is demonstrated by several analysis examples. A standard procedure for topology optimization could be applied to the FSI problem. From the solved optimization examples, the impact of the FSI effects could be observed.

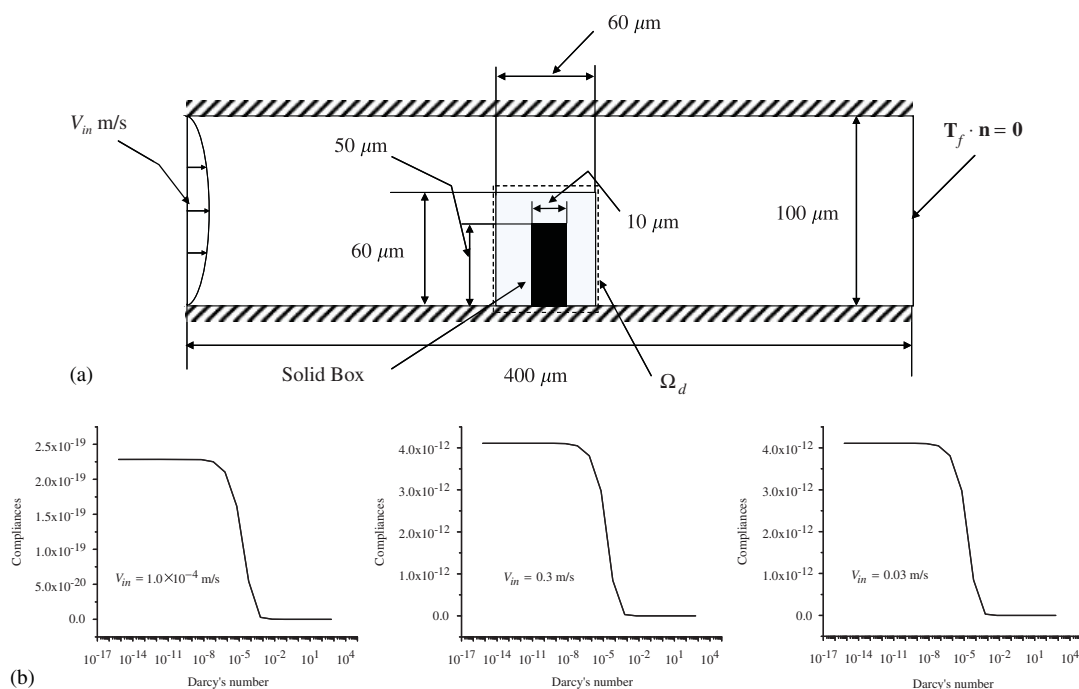


Figure 23. The compliance minimization problem for a small solid box due to the force of flow ( $\rho = 1000 \text{ kg/m}^3$ ,  $\mu = 0.001 \text{ kg m}^{-1} \text{ s}^{-1}$ ,  $E = 3 \times 10^9 \text{ N/m}^2$ ,  $\nu = 0.3$ , Mass constraint: 10%). (a) The first problem definition and (b) the compliance curve with various Darcy's numbers.

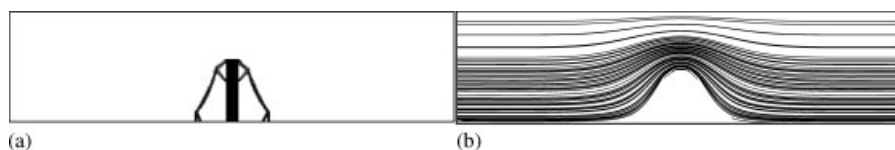


Figure 24. An obtained result for the compliance minimization problem with a slow flow. ( $V_{in} = 1.0 \times 10^{-4} \text{ m/s}$ ,  $Da = 10^{-9}$ ): (a) an obtained design (Object =  $3.4025 \times 10^{-20} \text{ J}$ ,  $Re = 0.004$ ) and (b) the flowlines.

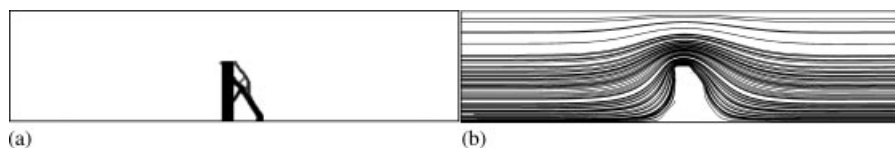


Figure 25. An obtained result for the compliance minimization problem with a faster flow. ( $V_{in} = 0.03 \text{ m/s}$ ,  $Da = 10^{-9}$ ): (a) an obtained design (Object =  $2.4741 \times 10^{-15} \text{ J}$ ,  $Re = 12$ ) and (b) the flowlines.

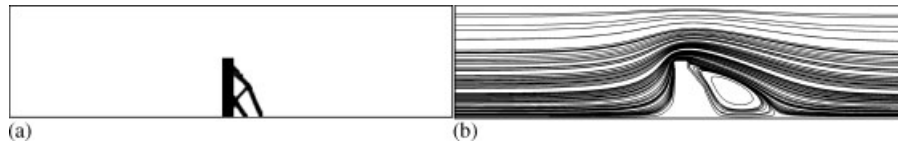


Figure 26. An obtained result for the compliance minimization problem with a fastest flow. ( $V_{in}=0.3$  m/s,  $Da=10^{-9}$ ): (a) an obtained design (Object= $6.2448 \times 10^{-13}$  J,  $Re=120$ ) and (b) the flowlines.

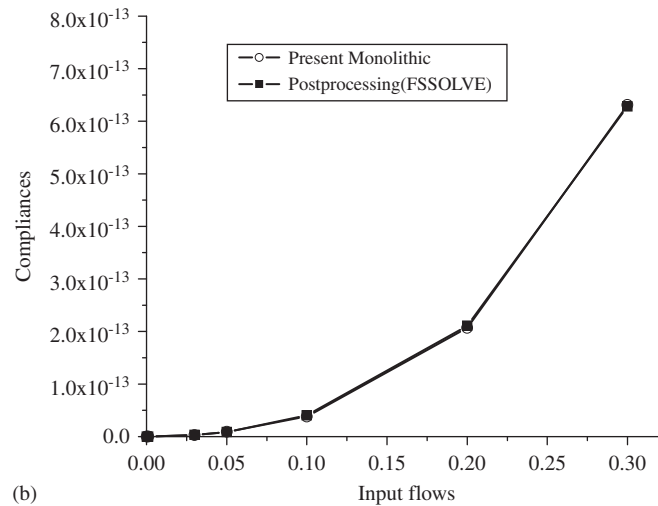
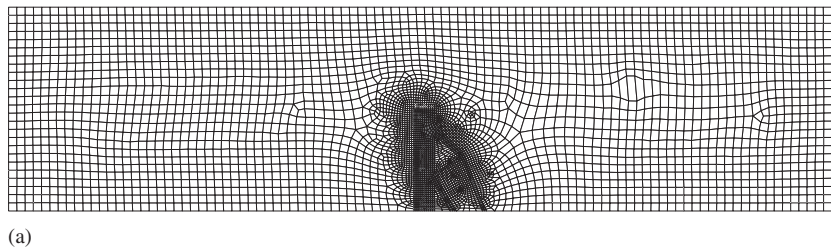


Figure 27. Verifications of the obtained designs with the staggered analysis method: (a) an used finite element model in FSSOLVE and (b) comparisons of compliances.

Some areas deserve further study in relation to the FSI problems. First, we believe that the presented approach can be extended to a transient FSI system by using the level set-based geometry interpretation and the smoothed particle hydrodynamics (SPH) method. Second, it may be possible to incorporate the geometrical non-linearities to simulate large displacements and flow-induced oscillations (referred to as flatter). Furthermore, a more important variability can be expected if a remeshing algorithm or a mesh regulation algorithm is considered.



## ACKNOWLEDGEMENTS

This work was supported by the Korea Research Foundation Grant funded by the Korean Government (KRF-2008-331-D00013).

## REFERENCES

1. Bendsøe MP, Sigmund O. *Topology Optimization Theory, Methods and Applications*. Springer: Berlin, 2003.
2. Yoon GH, Sigmund O. A monolithic approach for electrostatic problems. *Computer Methods in Applied Mechanics and Engineering* 2008; **197**(45–48):4062–4075.
3. Sigmund O. Design of multiphysics actuators using topology optimization—Part I: one material structure. *Computer Methods in Applied Mechanics and Engineering* 2001; **190**(49–50):6577–6604.
4. Yamamoto T, Maruyama S, Nishiwaki S, Yoshimura M. Topology design of multi-material soundproof structures including poroelastic media to minimize sound pressure levels. *Computer Methods in Applied Mechanics and Engineering* 2009; **198**(17–20):1439–1455.
5. Choi JS, Yoo JH. Structural optimization of ferromagnetic materials based on the magnetic reluctivity for magnetic field problems. *Computer Methods in Applied Mechanics and Engineering* 2008; **197**(49–50):4193–4206.
6. Yoon GH, Kim YY. Element connectivity parameterization for topology optimization of geometrically nonlinear structures. *International Journal of Solids and Structures* 2005; **42**(7):1983–2009.
7. Yoon GH, Kim YY. The element connectivity parameterization formulation for the topology design optimization of multiphysics systems. *International Journal for Numerical Methods in Engineering* 2005; **64**:1649–1677.
8. Hammer VB, Olhoff N. Topology optimization of continuum structures subjected to pressure loading. *Structural and Multidisciplinary Optimization* 2000; **19**:85–92.
9. Sigmund O, Clausen PM. Topology optimization using a mixed formulation: an alternative way to solve pressure load problems. *Computer Methods in Applied Mechanics and Engineering* 2007; **196**:1874–1889.
10. Yoon GH, Jensen JS, Sigmund O. Topology optimization of acoustic-structure interaction problems using a mixed finite element formulation. *International Journal for Numerical Methods in Engineering* 2007; **70**:1049–1076.
11. Bruggi M, Cini C. An alternative truly-mixed formulation to solve pressure load problems in topology optimization. *Computer Methods in Applied Mechanics and Engineering* 2009; **198**(17–20):1500–1512.
12. Rochus V, Rixen DJ, Golinval JC. Monolithic modelling of electro-mechanical coupling in micro-structures. *International Journal for Numerical Methods in Engineering* 2006; **65**:461–493.
13. Maute K, Allen M. Conceptual design of aeroelastic structures by topology optimization. *Structural and Multidisciplinary Optimization* 2004; **27**(1–2):27–42.
14. Pingen G, Evgrafov A, Maute K. Topology optimization of flow domains using the lattice Boltzmann method. *Structural and Multidisciplinary Optimization* 2007; **34**:507–524.
15. Fridolin O, Henrik B. Design of microfluidic bio-reactors using topology optimization. *European Conference on Computational Fluid Dynamics ECCOMAS CFD*, Netherlands, 2006.
16. Park KJ, Lee JN, Park GJ. Structural shape optimization using equivalent static loads transformed from dynamic loads. *International Journal for Numerical Methods in Engineering* 2005; **63**:589–602.
17. Xiaodong W. Instability analysis of some fluid–structure interaction problems. *Computers and Fluids* 2003; **32**:121–138.
18. Xiaodong W. Analytical and computational approaches for some fluid–structure interaction analyses. *Computers and Structures* 1999; **72**:423–433.
19. Frederic JB. A monolithic fluid–structure interaction algorithm applied to the piston problem. *Computer Methods in Applied Mechanics and Engineering* 1998; **167**:369–391.
20. Legay A, Chessa J, Belytschko T. An Eulerian–Lagrangian method for fluid–structure interaction based on level sets. *Computer Methods in Applied Mechanics and Engineering* 2006; **195**:2070–2087.
21. Vierendeels J, Dumont K, Verdonck PR. A partitioned strongly coupled fluid–structure interaction method to model heart valve dynamics. *Journal of Computational and Applied Mathematics* 2008; **215**:602–609.
22. Gerstenberger A, Wolfgang AW. An extended finite element method/lagrange multiplier based approach for fluid–structure interaction. *Computer Methods in Applied Mechanics and Engineering* 2008; **197**:1699–1714.
23. Gordon CE, Francis MH. Coupled finite element/boundary element approach for fluid-s-structure interaction. *The Journal of the Acoustical Society of America* 1990; **87**:1938–1947.
24. Luca H. On the stability of the finite element immersed boundary method. *Computers and Structures* 2008; **86**:598–617.

25. Greenshields CJ, Weller HG. A unified formulation for continuum mechanics applied to fluid–structure interaction in flexible tubes. *International Journal for Numerical Methods in Engineering* 2005; **64**(12):1575–1593.
26. Park KC, Felippa CA, Ohayon R. Partitioned formulation of internal fluid–structure interaction problems by localized Lagrange multipliers. *Computer Methods in Applied Mechanics and Engineering* 2001; **190**:2989–3007.
27. Felippa CA, Park KC, Farhat CA. Partitioned analysis of coupled mechanical systems. *Computer Methods in Applied Mechanics and Engineering* 2001; **190**:3247–3270.
28. Loon RV, Anderson PD, van de Vosse FN, Sherwin SJ. Comparison of various fluid–structure interaction methods for deformable bodies. *Computers and Structures* 2007; **85**:833–843.
29. Zhang LT, Gay M. Immersed finite element method for fluid–structure interactions. *Journal of Fluids and Structures* 2007; **23**:839–857.
30. Peskin CS. Numerical analysis of blood flow in the heart. *Journal of Computational Physics* 1977; **25**:220–252.
31. Lund E, Moller H, Jakobsen LA. Shape design optimization for steady fluid–structure interaction problems with large displacements. *Structural and Multidisciplinary Optimization* 2003; **25**:383–392.
32. Borrvall T, Petersson J. Topology optimization of fluids in stokes flow. *International Journal for Numerical Methods in Fluids* 2003; **41**:77–107.
33. Guest JK, Prevost JH. Topology optimization of creeping fluid flows using a Darcy–Stokes finite element. *International Journal for Numerical Methods in Fluids* 2006; **66**:461–484.
34. Gersborg-Hansen A, Sigmund O, Harber RB. Topology optimization of channel flow-problems. *Structural and Multidisciplinary Optimization* 2005; **30**(3):181–192.
35. Olesen LH, Okkels F, Bruus H. A high-level programming-language implementation of topology optimization applied to steady-state Navier–Stokes flow. *International Journal for Numerical Methods in Engineering* 2006; **65**(7):975–1001.
36. Bruns TE. Topology optimization of convection-dominated, steady-state heat transfer problems. *International Journal of Heat and Mass Transfer* 2007; **50**:2859–2873.
37. Duan XB, Ma YC, Zhang R. Shape-topology optimization of stokes flow via variational level set method. *Applied Mathematics and Computation* 2008; **202**(1):200–209.
38. Duan XB, Ma YC, Zhang R. Shape-topology optimization for Navier–Stokes problem using variational level set method. *Journal of Computational and Applied Mathematics* 2008; **222**(2):487–499.
39. Amstutz S, Andra H. A new algorithm for topology optimization using a level-set method. *Journal of Computational Physics* 2005; **216**:573–588.
40. ANSYS User's Manual. Swanson Analysis Systems, Inc. Houston, PA, 1995.
41. Cook RD, Malkus DS, Plesha ME, Witt RJ. *Concepts and Applications of Finite Element Analysis*. Wiley: New York, 2001.
42. Bathe KJ. *Finite Element Procedures*. Prentice-Hall: Englewood Cliffs, 1996.
43. Liu Q, Vasilyev OV. A Brinkman penalization method for compressible flows in complex geometries. *Journal of Computational Physics* 2007; **227**(2):946–966.
44. Brinkmann HC. A calculation of the viscous force exerted by a flowing fluid on a dense swarm of particles. *Applied Scientific Research* 1949; **1**(1):27–34.
45. Svanberg K. The method of moving asymptotes—a new method for structural optimization. *International Journal for Numerical Methods in Engineering* 1987; **24**:359–373.
46. COMSOL Reference Manual. COMSOL, 2007.